submitted to *Earth and Space Science*

Planetary Neutron Spectroscopy for Metal-rich Compositions: Development of Analysis Framework for Measurements at the Asteroid (16) Psyche

David J. Lawrence, John O. Goldsten, Patrick N. Peplowski, and Zachary W. Yokley
Johns Hopkins University Applied Physics Laboratory, Laurel, MD

Andrew W. Beck
Marietta College, Marietta, OH

Morgan T. Burks
Lawrence Livermore National Laboratory, Livermore, CA

Linda Elkins-Tanton
Arizona State University, Tempe, AZ

Insoo Jun
NASA Jet Propulsion Laboratory, Pasadena, CA

Timothy J. McCoy
Smithsonian Institution, Washington, DC

Thomas H. Prettyman
Planetary Science Institute, Tucson, AZ

Abstract

Neutron spectroscopy has become a standard technique for remotely measuring planetary surface compositions from orbital spacecraft around various planets. Measurements have successfully been carried out at the Moon, Mars, Mercury, and the asteroids Vesta and Ceres. The NASA Psyche mission is planning to make neutron measurements to characterize the composition of the M-class asteroid (16) Psyche. Earth-based remote sensing measurements allow for a wide

range of Fe concentrations, ranging from ~25 wt.% to 90 wt.%, and geochemically plausible Ni concentrations range from 0 wt.% to 10 wt.% or higher. To prepare for the analysis of Psyche neutron data, we have developed a new principal component analysis framework using four neutron energy ranges of thermal, low-energy epithermal, high-energy epithermal, and fast neutrons. With this analysis framework, we have demonstrated that the neutron measurements can uniquely distinguish variations of metal-to-silicate fraction, Ni, and hydrogen compositions. The strongest principal component is that of metal-to-silicate; the second strongest is Ni variations; the third is hydrogen variations. The validity of this framework can be first tested during a Mars gravity assist prior to arrival at Psyche.

1. Introduction

Planetary neutron spectroscopy has become a standard technique for remotely measuring the elemental composition of planetary surfaces from orbit. Neutrons are generated by nuclear spallation reactions from galactic cosmic rays (GCRs) on airless or nearly airless planetary surfaces. This technique was originally suggested by [*Lingenfelter et al.*, 1961], and measurements of planetary neutrons were first accomplished with NASA's Lunar Prospector (LP) mission, which separately measured thermal (neutron energy E_n<0.4 eV), epithermal (0.4<E_n<~10 keV), and fast (E_n>500 keV) neutrons [*Feldman et al.*, 1998a; 1998b]. Subsequent neutron measurements have been made at Mars [e.g., *Feldman et al.*, 2011; *Maurice et al.*, 2011], Mercury [e.g., *Lawrence et al.*, 2013a; *Lawrence et al.*, 2017], and the asteroids Vesta and Ceres [e.g., *Prettyman et al.*, 2012; 2017].

Compositional information of planetary surfaces is acquired via different energy ranges of the leakage neutrons. The lowest energy range (thermal neutrons) provides sensitivity to variations in strongly neutron-absorbing elements. On typical planetary surfaces, major elements that are strong neutron absorbers include Fe and Ti [*Feldman et al.*, 1998a]. Minor elements that are strong neutron absorbers are Cl and Ni, and these elements can affect thermal neutron measurements when they have sufficiently high concentrations (e.g., Mars, Psyche). Finally, there are trace rare-earth elements (e.g., Gd and Sm) that cause thermal-neutron variations when these elements have concentrations of tens of ppm [*Elphic et al.*, 2000].

Medium energy neutrons (or epithermal neutrons) primarily have sensitivity to variations in hydrogen (H) due to the strong neutron moderation that occurs with H. Depending on the sensors

used for detection, epithermal neutrons are also sensitive to variations in rare-earth elements [*Lawrence et al.*, 2006]. The highest energy range (or fast neutrons) has sensitivity to variations in average atomic mass (<A>). On typical planetary surfaces, the elemental variations that drive fast-neutron variability are generally Fe, Al, Mg, and O [*Lawrence et al.*, 2017]. For large H concentrations (>few hundred parts per million [ppm]), fast neutrons show variations due to neutron moderation and are sensitive to depth variations of H concentrations up to tens of cm [*Feldman et al.*, 2007].

The NASA Psyche mission to the asteroid (16) Psyche broadens the expected phase space of neutron measurements with the possibility of very high Fe abundances (up to 90 wt.%) and up to ~10 wt.% or greater Ni [*Elkins-Tanton et al.*, 2020]. Such high metal abundances will significantly affect the leakage neutron flux and therefore require a new assessment of how to carry out and interpret neutron data. Additionally, the Psyche neutron spectrometer will separately sample four different neutron energy bands, providing a larger dataset than has been collected by prior neutron spectroscopy investigations. Towards this end, we present a new analysis framework where the different compositional variabilities expected on Psyche can be identified and quantified. For this study, we provide an overview of possible Psyche compositions and how they relate to neutron spectroscopy measurements (Section 2); provide a summary of the planned Psyche neutron measurements (Section 3); and finally, present simulated neutron fluxes, predicted neutron count rates, and a principal component analysis framework that can be used to analyze and interpret the expected Psyche neutron data (Section 4).

2. Possible (16) Psyche Composition: Elements Relevant to Neutron Spectroscopy

One of the primary science objectives of the Psyche mission is to measure the asteroid Psyche's elemental composition to determine if it is a remnant core of a protoplanetary body [*Elkins-Tanton et al.*, 2020]. To accomplish this objective, the mission includes a Gamma-Ray and Neutron Spectrometer (GRNS) that will measure Psyche's elemental composition for a number of elements (Fe, Ni, Si, K, Al, Ca, and S) using a Gamma-Ray Spectrometer (GRS), and will measure complementary compositional parameters using a Neutron Spectrometer (NS) [*Lawrence et al.*, 2019].

A key goal of the Psyche neutron measurements is to quantify the asteroid metal-to-silicate fraction. When discussing "metal-to-silicate fraction" for gamma-ray and neutron spectroscopy,

an important distinction needs to be understood. For typical meteorite science investigations, metal-to-silicate fraction is defined as the total amount of metal (e.g., metallic iron and nickel) versus total silicates (elements bound as oxides). Thus, in the standard geochemical definition, oxidized iron (e.g., FeO) is "book kept" with silicates. In contrast, gamma-ray and neutron spectroscopy is sensitive elemental composition independent of the material's mineralogical state. For Psyche, the largest concentration of "metal" elements being considered consist of Fe and Ni; we therefore define the "metal" content as the total concentration of Fe and Ni, regardless of its mineral host. Silicates are defined as materials containing other major rock-forming elements (Si, O, Al, Mg, Ca, etc.). The silicate fraction as defined here is a compositional parameter that can be specified for any mixture of minerals (see Table 2) and determined using neutron spectroscopy.

On typical planetary bodies, the elements that primarily affect neutron measurements are Fe, Ti, Cl, Ni, Gd, Sm, and H, as well as elements with contrasting <A> (see Section 1). Recent Earth-based measurements and new interpretations of existing measurements have revised our understanding of the nature of Psyche, and the currently accepted density of Psyche is bounded to be 3.4–4.1 g/cm^3 [*Elkins-Tanton et al.*, 2020]. Psyche's Fe abundances could plausibly range from 25 wt.% to upwards of 90 wt.%, and by consequence, the silicate fraction could range from less than 0.1 to greater than 0.7. Meteoritic analogs for Psyche therefore include iron meteorites as well as metal-rich meteorites such as CB and enstatite chondrites, pallasites, and mesosiderites [*Peplowski et al.*, 2019]. If Psyche is related to iron meteorites, then it must have significantly higher porosity than is typical for >100-km-diameter asteroids, or retain a significant fraction of the silicate shell, given the relatively low density. The wide range of compositions suggest that additional elements including Mg, C, P, and Co, may be geochemically important [*Peplowski et al.*, 2019] and thus we include them when modeling expected neutron fluxes.

Another element that has gained increased importance at Psyche is H. Ground-based measurements using the NASA Infrared Telescope Facility have detected a 3-μm absorption on Psyche that is consistent with hydration features attributed to OH and H_2O bearing phases [*Takir et al.*, 2017]. By analogy to the basaltic asteroid 4 Vesta [*Prettyman et al.*, 2012], this H may be due to exogenous, water-rich carbonaceous-chondritic material accumulated on its surface. Based on a cross correlation of Earth-based data from both Vesta and Psyche with orbital H measurements at Vesta, *Reddy et al.* [2018] estimated that the bulk hydrogen concentrations could be in the range of 200 – 300 ppm, which is comparable to the range of H variations (0 – 400 ppm)

seen at Vesta [*Prettyman et al.*, 2012; *Lawrence et al.*, 2013b]. While not needed to directly address the mission's science objectives, H in this abundance range can affect the measured neutron composition parameters [*Lawrence et al.*, 2013b; *Prettyman et al.*, 2013], as well as gamma-ray data when making composition measurements using both capture and inelastic gamma-ray lines [*Yamashita et al.*, 2013; *Peplowski et al.*, 2015a; *Wilson et al.*, 2019]. Thus, effects from bulk H concentrations and its possible spatial variability need to be taken into account with the measured GRNS data.

3. The Psyche GRNS and Neutron Flux Environment at Psyche

The Psyche GRNS consists of two sensor subsystems that separately measure gamma rays and neutrons [*Lawrence et al.*, 2019]. The GRS uses a cryocooled high-purity Ge (HPGe) sensor to measure gamma rays with high precision and excellent energy resolution (≤3.5 keV @ 1332 keV). The HPGe sensor is surrounded by a borated plastic scintillator anticoincidence (AC) shield that both provides active background rejection from charged particles for the gamma-ray measurements, as well as fast-neutron measurements due to its 5 wt. % boron loading. As with the MESSENGER GRS [*Peplowski et al.*, 2015b], the AC shield has a solid "puck" (7.75 cm radius and 5.76 cm tall) and cylindrical annulus (1.75 cm thick and 8.8 cm tall). The NS consists of three, identical ^{3}He gas proportional sensors (5.08-cm diameter, 25.41-cm long active length, 10-atmosphere pressure)[*Peplowski et al.*, 2020] that use different material coverings to discriminate three separate neutron energy ranges (Figure 1). Thermal and low-energy epithermal neutrons are measured using a bare sensor and a 0.05 cm-thick Cd-covered sensor; high-energy epithermal (~1 keV < E_n < 500 keV) neutrons are measured with a polyethylene-covered (1-cm thick) ^{3}He sensor. As a consequence, the term "neutron sensors" includes the NS subsystem, along with the borated plastic scintillator from the GRS subsystem.

The energy-dependent response of the neutron sensors is shown in Figure 2. The lowest energy thermal neutrons are detected with two ^{3}He sensors, as was done for the Lunar Prospector mission [*Feldman et al.*, 2004]. The bare ^{3}He sensor detects the combined flux of thermal plus epithermal neutrons, and the Cd-covered ^{3}He sensor detects epithermal neutrons. The Cd-covered sensor uses a 0.05-cm-thick layer of Cd, which absorbs all neutrons with energies less than 0.4 eV. Thermal neutrons are thus measured as the count-rate difference between the bare and Cd-covered sensors. The third sensor is covered in a 1-cm-thick layer of polyethylene to increase sensitivity for high-

156 energy-epithermal neutrons. Detection of high-energy-epithermal neutrons is used to optimize
157 neutron measurements at Psyche to account for the possibly higher Fe and Ni content than any
158 other planetary body for which neutron measurements have been made, as well as variable H
159 concentrations.
160 A very high metal content (up to 90 wt.% Fe) will significantly modify the emitted neutron
161 flux compared to bodies with rocky silicate-rich materials. Modeled neutron fluxes for various
162 permutations of metal-to-silicate fractions and H concentrations are shown in Figure 3. When the
163 metal fraction is increased (Figure 3A), the thermal neutron flux is suppressed, and the high-energy
164 neutron flux is enhanced. Thermal neutrons are suppressed because both Fe and Ni are highly
165 efficient absorbers of thermal neutrons. The microscopic neutron absorption cross sections (at
166 0.025 eV) for the most abundant Fe and Ni isotopes ^{56}Fe and ^{58}Ni are 2.6 and 4.2 barn (10^{-24} cm^2),
167 respectively. These values compare to neutron absorption cross sections that range from 10^{-4} to
168 0.6 barn for other common elements in silicate materials (e.g., O, Si, Al, Ca, Mg). The fluxes of
169 high-energy epithermal and fast neutrons are correspondingly enhanced for increasing metal
170 content because for both energy ranges, larger neutron fluxes are generated for materials with
171 larger average atomic mass (<A>) [*Gasnault et al.*, 2001; *Lawrence et al.*, 2011]. The largest
172 metal-to-silicate fractions considered for possible Psyche-like materials have <A> values around
173 ~40–50 atomic mass units (amu), compared to ~20–25 amu for typical silicate materials. It should
174 be noted that because the per-nucleon-binding energy of Ni is higher than Fe, the neutron
175 separation energy is likewise higher and thus liberation of neutrons during nuclear spallation of Ni
176 is inhibited, relative to Fe [*Peplowski et al.*, 2018]. Thus, for materials with large Ni
177 concentrations, there will be a breakdown of the well-known correlation between fast neutron
178 production and average atomic mass [*Gasnault et al.*, 2001].
179 In addition to metal content, variable H concentrations will cause neutron-flux changes that
180 need to be considered when analyzing and understanding the neutron data. As mentioned in
181 Section 2, H is likely present on Psyche at hundreds of ppm [*Reddy et al.*, 2018] and possibly has
182 variable concentrations across its surface [*Sanchez et al.*, 2017]. Typically, H is measured using
183 the low-energy portion of epithermal neutrons ranging from 0.3 eV to ~1–10 keV [*Feldman et al.*,
184 1998b]. For metal-rich compositions with varying H concentrations, this low-energy epithermal
185 energy range has little sensitivity to H concentrations, and the energies sensitive to H are shifted
186 to higher energies of 10 keV to a few hundred keV (Figure 3B). Thus, while the Cd-covered ^{3}He

neutron sensor provides the needed background subtraction for the bare ^{3}He sensor, it will not provide a sensitive measure of H concentrations for a metal-rich body. The polyethylene covered ^{3}He sensor provides an order-of-magnitude increased sensitivity to high-energy epithermal neutrons (Figure 2) compared to either the bare or Cd covered sensors.

4. Deriving Compositional Variations with Psyche Neutron Data

The Psyche GRNS provides four neutron measurables of thermal, low-energy epithermal, high-energy epithermal, and fast neutrons. Here, we describe particle transport simulations to estimate the performance of these neutron measurements for a range of plausible Psyche compositions. The neutron production was simulated by illuminating a Psyche sized body with a GCR proton flux using the particle transport code MCNPX, which has a long history of application for planetary nuclear spectroscopy applications [e.g., *Prettyman et al.*, 2006]. Using the sensor energy-dependent responses shown in Figure 2, simulations were carried out to calculate the expected neutron count rates for a range metal-to-silicate ratios, Ni concentrations, and H concentrations. Metal concentration ranged from 10 to 90 vol.% metal in steps of 10 vol. %; Ni abundances ranged from 2 wt.% to 30 wt.% Ni in steps of 2 wt.%; and H abundances ranged from 0 to 500 ppm H in steps of 100 ppm. Metal is nominally defined using IVA iron-meteorite composition with 8.4 wt.% Ni, the remainder Fe, and silicates are defined as Mg-rich orthopyroxene (bronzite - – $Mg_{0.87}Fe_{0.13}SiO_3$), as has been predicted to exist on Psyche [*Hardersen et al.*, 2005]. Bulk compositions from various vol.% fractions of metal and bronzite were calculated using modal recombination analysis [*Berlin et al.*, 2008], thus accommodating for the large density contrast between metal and silicate. While the silicate ($Mg_{0.87}Fe_{0.13}SiO_3$) contribution to Fe_{total} is insignificant with moderate or high vol.% metal, when metal becomes very low in concentration, we acknowledge that Fe_{total} would largely be controlled by silicate composition.

In total, 840 simulated neutron spectra were calculated from which neutron count rates were derived. In order to approximate the expected measured count rates at Psyche, the modeled count rates from the bare and Cd-covered ^{3}He sensors were scaled to the measured and modeled count rates from the similar sensors from the LP-NS using a lunar highlands material [*Lawrence et al.*, 2006], accounting for differences in geometry between the lunar measurements and those planned for Psyche's low-attitude mapping orbit. The count rates for the polyethylene covered ^{3}He sensor

were obtained by scaling the relative energy-integrated responses of the polyethylene- and Cd-covered ^{3}He sensors. The count rates for the fast neutron sensor were obtained by scaling the count rate from the MESSENGER NS fast neutron sensor at Mercury [*Lawrence et al.*, 2013a; 2017], which has a similar size to the Psyche GRS borated plastic scintillator. The count rates were scaled to an assumed altitude of one Psyche radius. A full understanding and calibration of all the neutron sensors will be obtained after the complete instrument calibration measurements are completed. Additional benchmarking and calibration will be accomplished using flight data from the Mars gravity assist.

Figure 4 shows count-rate plots for the six different permutations of thermal, low-energy epithermal, high-energy epithermal, and fast neutrons. In each plot, lines of constant metal-to-silicate fraction and constant Ni are given by the red and black lines, respectively. The red/black contours show the count rates for 0 ppm H; the gray contours show count rates for 500 ppm H. Each sensor combination provides different information about the three composition measurables of metal-to-silicate fraction (or silicate fraction), Ni abundances, and H abundances. For example, the combination of thermal versus fast neutrons (Figure 4A) provides a good measure of silicate fraction. Specifically, high thermal and low fast neutron count rates indicate a high silicate fraction, and the reverse (low thermal and high fast neutron count rates) indicate low silicate fraction. This behavior is also clearly observed in the neutron fluxes given in Figure 3A. However, with variable and/or uncertain H abundances, the thermal versus fast neutron count-rate combination would do a poor job of constraining Ni concentrations, as there is significant overlap for count rates with variable H abundances. In contrast, the combination of fast versus high-energy epithermal neutrons (Figure 4B) can provide constraints on both silicate fraction and Ni abundances for variable H abundances, although there are still ambiguities. While we do not go into detail for the other measurement combinations, it is clear that each combination can provide some constraints on the compositional measurements, but also suffer from various ambiguities.

To simplify our understanding of this complex phase space of four neutron measurements and three compositional variables, we use an analysis technique known as Principal Component Analysis (PCA). PCA is a statistical technique where a set of partially correlated measurements – in this case the four neutron measurements – undergo a geometric-like transformation to generate a new set of variables that are formally uncorrelated. While one of the major benefits to PCA operations is to reduce the number of "important" variables, in this case PCA is used to maximize

compositional information while minimizing ambiguous overlap of measured data. Background information on PCA can be found in many places; a good overview is provided in [*Wilks*, 2011]. In addition, PCA has been used in a variety of planetary nuclear spectroscopy studies [*Chevrel et al.*, 2002; *Beck et al.*, 2015; *Peplowski and Stockstill-Cahill*, 2019].

For our purposes, we define a measurement vector $\boldsymbol{x} = [C_{\mathrm{therm}}, C_{\mathrm{lowE}}, C_{\mathrm{highE}}, C_{\mathrm{fast}}]$, where C represents the simulated count rates for each GRNS neutron sensor. The PCA was carried out using the *pcomp* function that is a part of the Interactive Data Language analysis package. The input to the function is a 4 x 840 element array of data vectors ($\boldsymbol{x}_m$, where m ranges from 0 to 839) that represents each of the 840 count-rate simulations (e.g., Figure 4). Using these input values, the *pcomp* function outputs a 4 x 4 element matrix, $\boldsymbol{E}$, that transforms each input data vector into a new principal component (PC) vector, $\boldsymbol{u}$:

$$\boldsymbol{u_m} = \boldsymbol{E}\boldsymbol{x_m} \quad (1)$$

In addition, the *pcomp* function outputs a four-element variance vector that quantifies the percentage of the total dataset variation (or weighting) for each principal component (PC) variable. One way to intuitively understand this PC process is that as in standard linear algebra or quantum mechanics, the PCs are eigenvectors, and their weighting values are the eigenvalues.

Results of the PCA are shown in Table 1 and Figure 5. Starting with Table 1, the first column shows the percentage variance contained in each PC. PC1 dominates the total variance at 95%, and the next two variables, PC2 and PC3, have variances comparable with each other at 3.5% and 1.1%, respectively. PC4 has a variance that is a factor of 18 lower than PC3. Thus, this PCA shows that over 99% of the variance in the four neutron measurables can be represented by only three PCs. The last four columns in Table 1 show the transformation matrix $\boldsymbol{E}$, such that each row indicates how each PC is a linear combination of all four neutron measurables. For example, the largest contributor to PC1 is the fast-neutron count rate with a coefficient of 0.865 followed by the thermal neutron count rate of -0.384. The positive fast-neutron coefficient indicates that the PC1 parameter increases when the fast-neutron count rate increases, and the negative thermal-neutron coefficient indicates that the PC1 parameter decreases when the thermal-neutron count rate increases. As is seen below, this is consistent with the observation that PC1 is strongly correlated with the silicate fraction compositional parameter. We also note that all neutron measurables have

a non-negligible contribution to PC1, thus indicating that all neutron measurements are needed to derive PC1.

Figure 5 shows three-dimensional scatter plots where each of the 840 x 4 element vectors have been transformed into PC space. The resulting data cloud is a stretched and curved parallelepiped-like volume. Most importantly, there are no overlapping data points as each is located in a unique position within the volume. To illustrate the compositional variability within this PC volume, each panel shows the data points color coded to represent the silicate fraction (Figure 5A), the Ni concentration (Figure 5B), and the hydrogen concentration (Figure 5C). PC1 is dominantly correlated with silicate fraction, PC2 is dominantly correlated with Ni concentration, and PC3 is dominantly correlated with H concentration. Thus, with an appropriate calibration, each of the PCs can be directly linked to a specific composition parameter.

The variations of the different PCs can be understood in terms of the elemental variations in the following manner. First, PC1, which positively correlates with silicate fraction, has an anticorrelation with thermal, low-energy, and high-energy epithermal neutrons; whereas it has a positive correlation with fast neutrons. This makes sense such that the neutron absorption due to the metal elements (Fe, Ni) cause the count rates from the three lowest energy bands to decrease (Note, even the high-energy epithermal-neutron sensor has a substantive response to low-energy neutrons where there is strong neutron absorption). In contrast, fast neutrons, which show increased count rates for larger metal count rates, has a strong positive correlation (0.865) with PC1. Second, PC2, which correlates with Ni abundances (Figure 5B), anticorrelates with all neutron measurables. These anticorrelations (especially the -0.817 value for thermal neutrons), makes sense because the low-energy neutron absorption for Ni is ~60% stronger than for Fe, the other metal constituent (Section 3). The negative correlations for fast, and possibly high-energy epithermal neutrons are likely due to the fact that neutron spallation from Ni is inhibited compared to the spallation from Fe [*Peplowski et al.*, 2018]. Finally, PC3, which negatively correlates with hydrogen abundances, has the strongest correlation with high-energy epithermal neutrons (0.838) as well as positive correlations with low-energy and fast neutrons. This indicates that as the hydrogen concentration goes up, the three highest-energy neutron measurements decrease, which is consistent with the fluxes shown in Figure 3B. In contrast, for increasing hydrogen content (decreasing PC3), the thermal neutrons increase, which is again consistent with Figure 3B.

While the PCA appears to be useful in interpreting these simulated neutron data, we recognize that these count rates were generated using an "artificial" bulk compositional framework, i.e., we used compositions that span the large ranges of silicate fraction, Ni and H concentrations, but we did not replicate the compositions of any specific meteorite or rock type. To test how this analysis framework represents known compositions, we calculated neutron fluxes for six different bulk meteoritic compositions. These are meteoritic compositions identified by *Peplowski et al.* [2019] and *Elkins-Tanton et al.* [2020] as spanning the likely possible values that will be observed at Psyche. The compositional values are given in Table 2 along with the associated silicate fractions. Figure 5D shows these count rates transformed into PC space. The PC values for these meteorite compositions are also given in Table 3. As seen, the PC1 values for these meteoritic compositions correlate closely with silicate fraction. This correlation is seen more clearly in Figure 6A where the PC1 value is plotted versus silicate fraction for the six meteoritic compositions. Variations in Ni abundances also track with PC2, which is more clearly seen in Figure 6B. We note, however, that since the contours of increasing Ni abundances are not strictly parallel to PC2, the correlation between PC2 and Ni abundance is not perfect. Nevertheless, when conducting a full analysis with flight data, a more exact correspondence between PC2 and Ni abundance can be derived in order to more accurately identify Ni abundances; this correspondence will be assisted by the direct and complementary Ni elemental composition data from the GRS [*Lawrence et al.*, 2019]. Finally, all of the meteoritic compositions contained no H, and as seen, their location within the PC data cloud is near the top of the volume (Figure 5D, which is consistent with the fact that they contain no H).

As a final check to test the usefulness of this PC analysis, we simulated the expected count rate of Mars crustal-like material [*Agee et al.*, 2013], which is relevant for the Psyche measurements because we expect to measure neutron fluxes from Mars during the Mars gravity assist while en-route to Psyche. These compositional values are also given in Table 2. While it is expected that the flyby geometry will be near Mars' equator, the longitudinal location is currently unknown as it depends on parameters like the exact Psyche mission launch date, which will not be known until it occurs. Nevertheless, Mars has a range of H concentrations across its equatorial region [*Maurice et al.*, 2011], so we used six instances of Mars crustal-like compositions with variable H concentrations ranging from 0.5 wt.% water equivalent hydrogen (WEH) to 9 wt.% WEH. The PC-transformed neutron count rates are shown as dark-red symbols in Figure 5D, separately in Figure 7 (PC3 versus WEH), and the values listed in Table 3. While Mars compositions are quite

different from the compositions considered in the original Psyche framework, they nevertheless show good consistency. Specifically, based on our definition of silicate fraction, the Mars points occur at low PC1 values, which is consistent with a high silicate fraction. Their PC2 values are quite low, consistent with the low Ni abundances within the Mars composition. Finally, the major variation is generally along the PC3 axis (Figure 7), which is consistent with the fact that the primary compositional variation in the Mars compositions is due to H.

5. Discussion and Summary

Given the wide range of possible elemental compositions of asteroid Psyche, neutron measurements from the asteroid include a high-energy epithermal neutron measurement to better constrain its compositional nature and variability. Using validated particle transport simulations with "artificial" compositions, we have shown that neutron flux variations due to metal-to-silicate, Ni, and H variations can be uniquely distinguished using a principal component analysis. Specifically, for our analysis PC1 was found to be sensitive to metal-to-silicate content, and PC2 was sensitive to Ni content. This same analysis has shown consistent results in distinguishing these three compositional variabilities for possible Psyche-like meteorite compositions as well as Mars compositions with variable H abundances.

As a first opportunity to test this framework, we note again that the Psyche mission is planning to carry out a Mars gravity assist prior to reaching Psyche, where the spacecraft will pass within a few hundred km of Mars' surface. All spacecraft science instruments are planning to operate through the gravity assist including the full GRNS. While not a required measurement, neutron data acquired at Mars would provide useful anchor points for the eventual measurements at Psyche. This is especially so because Mars' surface is well characterized with prior neutron measurements [*Maurice et al.*, 2011]. Thus, such Mars measurements could provide an early validation of the analysis framework presented here, and possibly provide revisions to our understanding of the full neutron data prior to reaching Psyche, should such revisions be necessary. We note that prior to applying this framework, all the neutron data (either at Mars or Psyche) need to be fully corrected for non-compositional observational variations as has been done in prior similar studies [*Maurice et al.*, 2004; 2011; *Prettyman et al.*, 2012]

In summary, planetary neutron data have provided essential composition information at all planetary bodies where such measurements have been made, e.g., the Moon, Mars, Mercury,

Vesta, and Ceres, which collectively span a wide range of iron, silicate, and H concentrations. Given that so little is currently known about Psyche, it is important to have multiple, independent ways to constrain its composition. GRNS neutron measurements will provide such compositional constraints, namely a robust measure of the silicate fraction, as well as constraints on the Ni fraction and surface H content.

Acknowledgements: The Psyche GRNS project is supported by the NASA Discovery Program under contracts 1569206 from NASA Jet Propulsion Laboratory and 17-256 from Arizona State University to the Johns Hopkins University Applied Physics Laboratory. Data archiving is underway, and will be made available at http://lib.jhuapl.edu/.

382

Table 1. Variance and PC parameters

	Variance	C_{therm}	C_{LowEpi}	C_{HiEpi}	C_{fast}
PC1	0.953	-0.384	-0.168	-0.272	0.865
PC2	0.035	-0.817	-0.103	-0.304	-0.479
PC3	0.011	-0.429	0.309	0.838	0.133
PC4	0.0006	0.017	-0.930	0.362	-0.060

383

384

385

Table 2. Table of mass fraction abundances for six meteorite types and Mars compositions. These abundance values were taken from [*Peplowski et al.*, 2019].

	Iron	**Pallasite**	**CB Chondrite**	**Mesosiderite**	**EH Chondrite**	**H Chondrite**	**Mars**
H	0.0	0.0	0.0	0.0	0.0	0.0	5.87×10^{-4}
C	0.0037	0.0	0.0	0.007	0.0039	0.0021	0.0
O	0.0	0.1722	0.129	0.214	0.3022	0.3533	0.4367
Na	0.0	0.0	0.0003	0.0009	0.0076	0.0	0.0291
Mg	0.0	0.1149	0.056	0.047	0.1101	0.1395	0.0494
Al	0.0	0.0	0.0063	0.021	0.0086	0.0105	0.0622
Si	0.0	0.0756	0.07	0.097	0.1731	0.1692	0.2332
P	0.0028	0.0030	0.0	0.0	0.0	0.0	0.0
S	0.0040	0.0089	0.0050	0.0270	0.0523	0.0198	0.0004
Cl	0.0	0.0	0.0	0.0	0.0	0.0	0.0023
K	0.0	0.0	0.0	0.0	0.0	0.0	0.0030
Ca	0.0	0.0011	0.0071	0.0148	0.0079	0.0121	0.0670
Ti	0.0	0.0	0.0	0.0	0.0	0.0	0.0062
Cr	0.0	0.0007	0.0030	0.0021	0.0032	0.0035	0.0013
Mn	0.0	0.0	0.0005	0.0016	0.0021	0.0023	0.0023
Fe	0.9170	0.5530	0.6740	0.5142	0.3113	0.2692	0.1060
Co	0.0046	0.0020	0.0022	0.0016	0.0008	0.0	0.0
Ni	0.0668	0.0685	0.0475	0.0510	0.0169	0.0169	0.0004
Sm	0.0	0.0	0.0	0.0	0.0	0.0	6.75×10^{-6}
Eu	0.0	0.0	0.0	0.0	0.0	0.0	1.66×10^{-6}
Gd	0.0	0.0	0.0	0.0	0.0	0.0	7.82×10^{-6}
Th	0.0	0.0	0.0	0.0	0.0	0.0	2.76×10^{-6}
U	0.0	0.0	0.0	0.0	0.0	0.0	5.38×10^{-7}
Silicate fraction	0.016	0.376	0.273	0.429	0.669	0.712	0.894

386

387

388

389

390

391

392

Table 3. PC values for the six meteorite compositions and Mars compositions with five separate water equivalent hydrogen (WEH) concentrations.

	PC1	PC2	PC3
Iron	10.0	-2.20	5.97
Pallasite	2.19	-2.12	5.78
CB Chondrite	3.33	-2.05	5.58
Mesosiderite	1.79	-2.20	5.72
EH Chondrite	0.178	-2.80	5.78
H Chondrite	-0.273	-3.10	5.92
Mars (0.65 wt.% WEH)	-1.23	-4.80	7.52
Mars (0.9 wt.% WEH)	-1.23	-4.74	7.15
Mars (1.8 wt.% WEH)	-1.25	-4.58	6.52
Mars (4.5 wt.% WEH)	-1.33	-4.22	5.58
Mars (9.0 wt.% WEH)	-1.37	-3.77	4.75

393

394

395

396

397

398

399

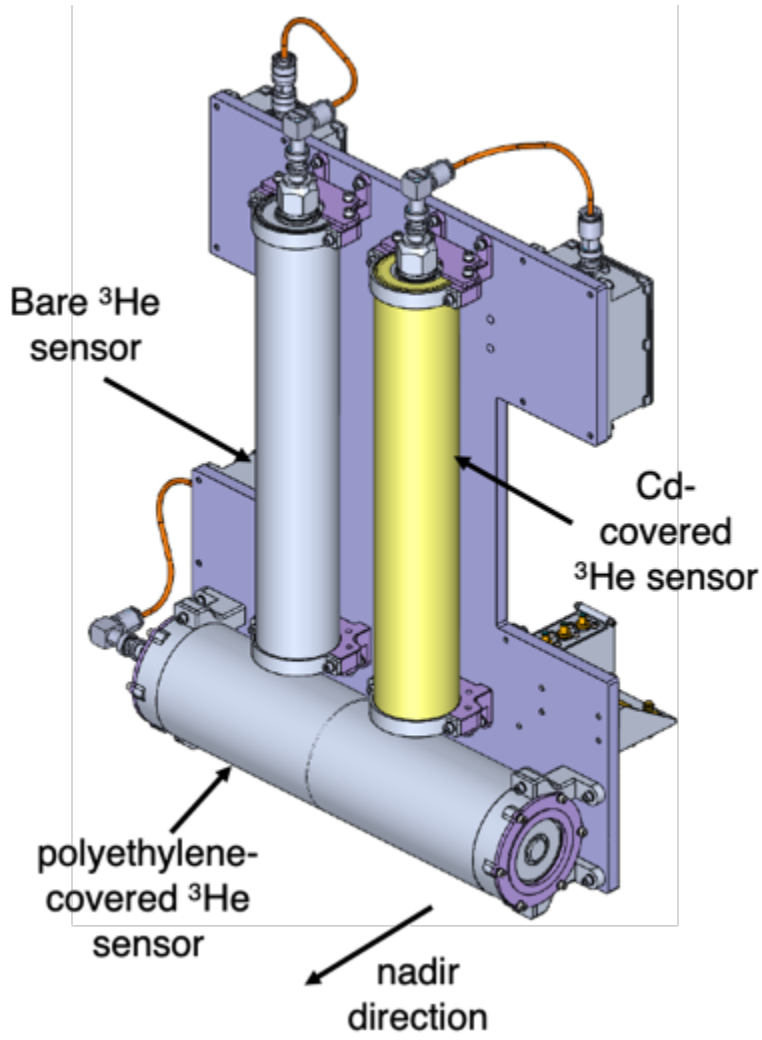

Figure 1. Psyche neutron spectrometer with three ^{3}He neutron sensors. The nadir direction that views Psyche is perpendicular to the cylinder axes of the sensors. Unlabeled components include pre-amplifier, high-voltage filter, harness connectors, and other instrument control functionality (e.g., thermal control). The length of each sensor assembly is ~30 cm.

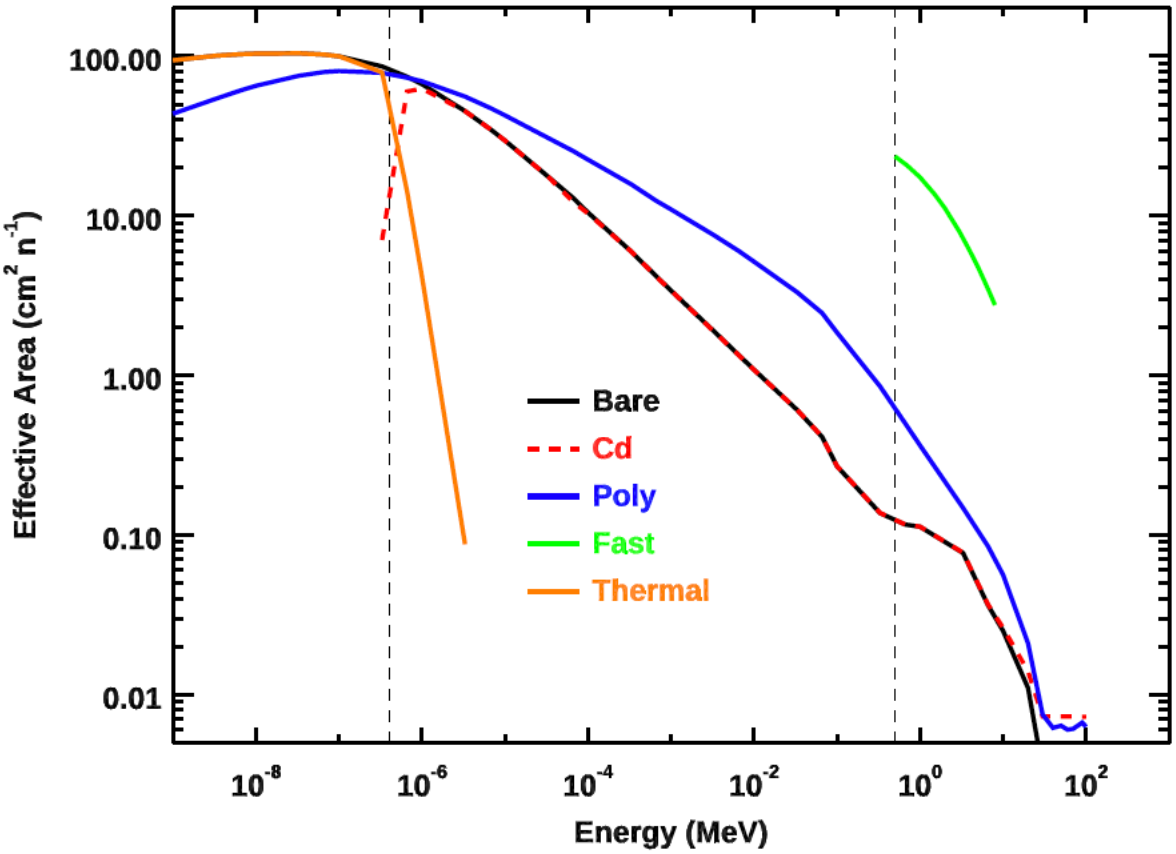

Figure 2. Modeled effective area (efficiency times area) for the four different neutron sensors that are part of the Psyche GRNS. The fast neutron effective-area is an estimate based on the efficiency calculated for the MESSENGER NS fast neutron sensor [*Lawrence et al.*, 2013a] combined with the cross-sectional area of the GRS AC shield (Section 3). The vertical, dashed lines indicate the standard energy boundaries for thermal to epithermal neutrons (0.4 eV), and epithermal to fast neutrons (0.5 MeV).

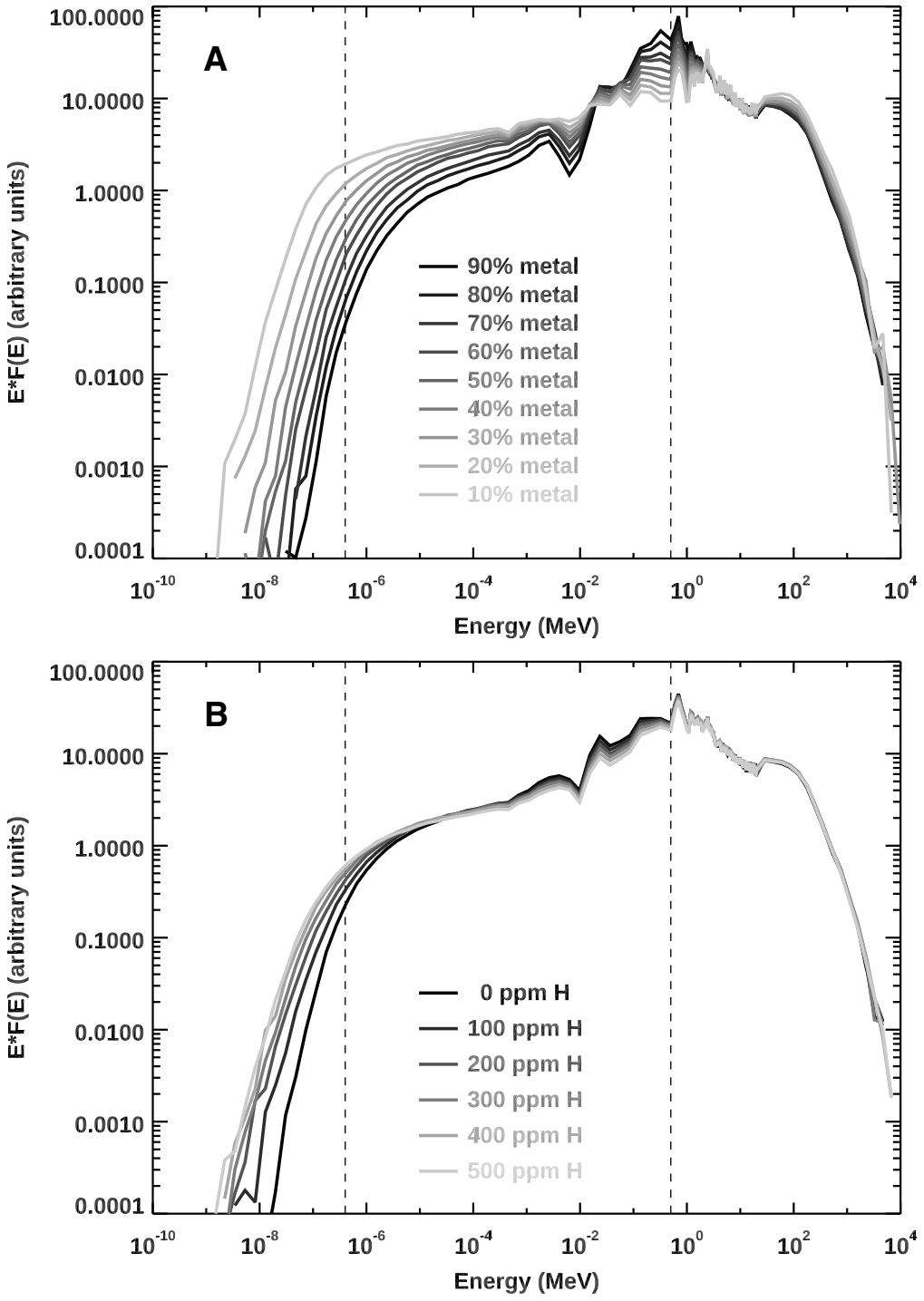

Figure 3. (A) Modeled neutron fluxes for range of metal-to-silicate compositions, with 8 wt.% Ni fraction within the metal; (B) and a range of hydrogen abundances within a metal-rich composition (0.9 metal fraction and 2 wt.% Ni within the metal). The vertical, dashed lines indicate the standard energy boundaries for thermal to epithermal neutrons (0.4 eV), and epithermal to fast neutrons (0.5 MeV).

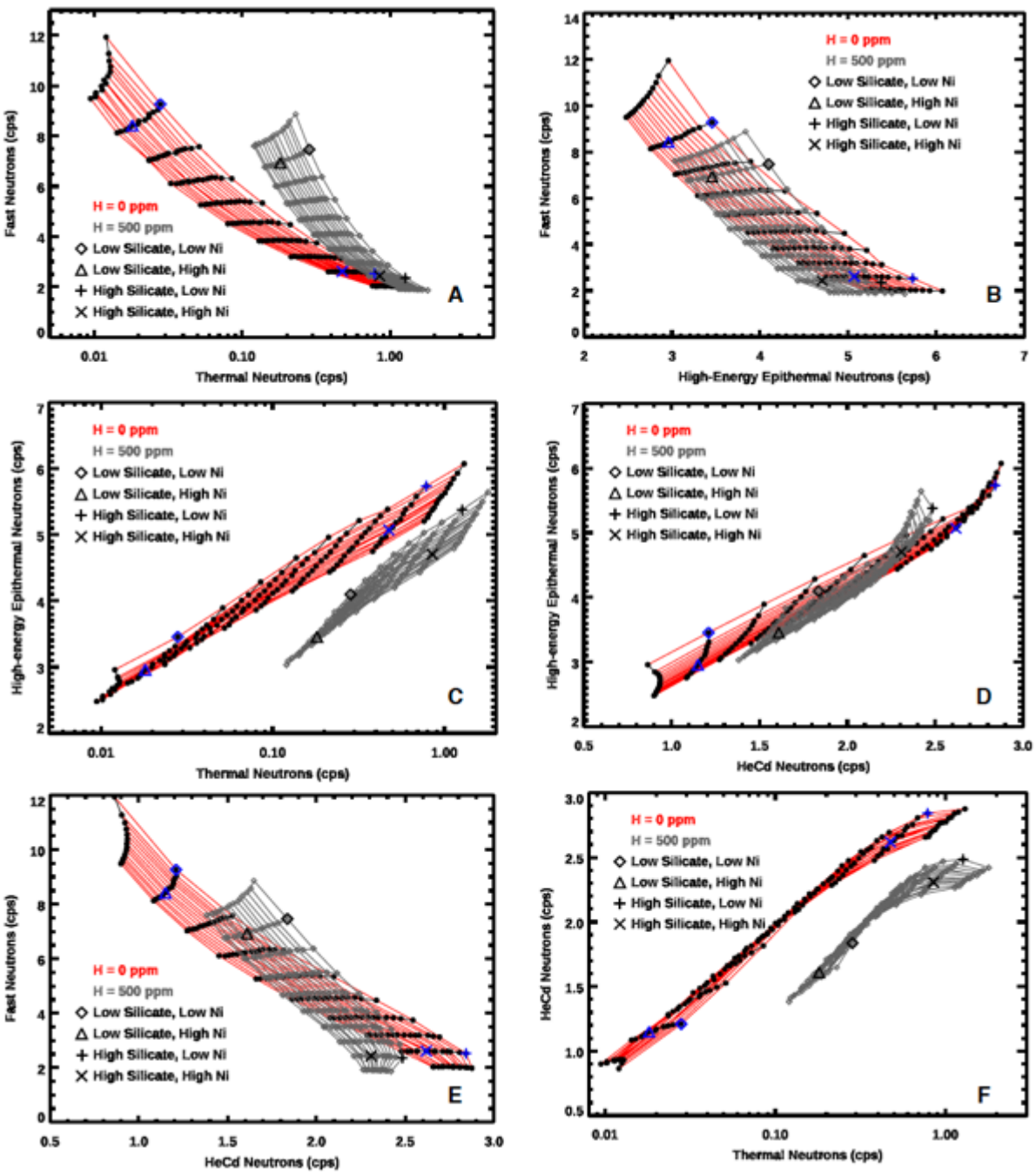

Figure 4. Simulated count-rate "feather plots" for all permutations of the four neutron measurements (A–F). 840 separate simulations were completed for a phase space of possible Psyche compositions ranging from 10 to 90 vol% silicates (or pyroxene), 2 to 30 wt.% Ni, and 0 to 500 ppm H. Contours of constant Ni abundances are given by the red lines; contours of constant silicate content are given by the black lines. Illustrative combinations of low silicate (20 vol. %), high silicate (80 vol.%), low Ni (2 wt.%) and high Ni (20 wt.%) are given by the symbols. The red and black feather plots use 0 ppm H, and the gray feather plots use 500 ppm H.

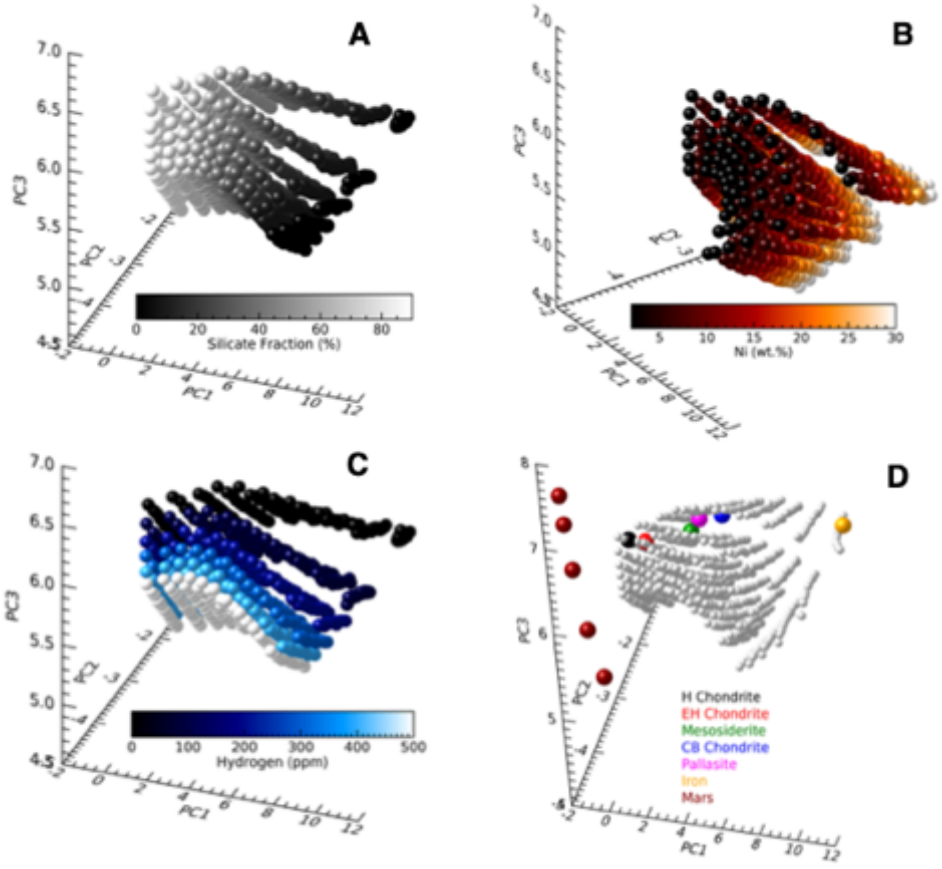

Figure 5. Three-dimensional scatterplot of the three principal components for the 840 neutron simulations for the range of silicate fraction, Ni concentrations, and hydrogen concentrations. While the axes rotations are different, the data points are in same locations for all panels. Data points are color coded based on silicate fraction (A), Ni concentration (B), and H concentration (C). Panel (D) shows the principal components for six different meteorite compositions (Table 2) along with six versions of Mars compositions with H concentrations of 0.5 wt.% (nominal value in Table 2), 0.9 wt.%, 1.8 wt.%, 4.5 wt.%, and 9 wt.% water equivalent hydrogen (WEH). Increasing values of WEH range from high to low PC3 values.

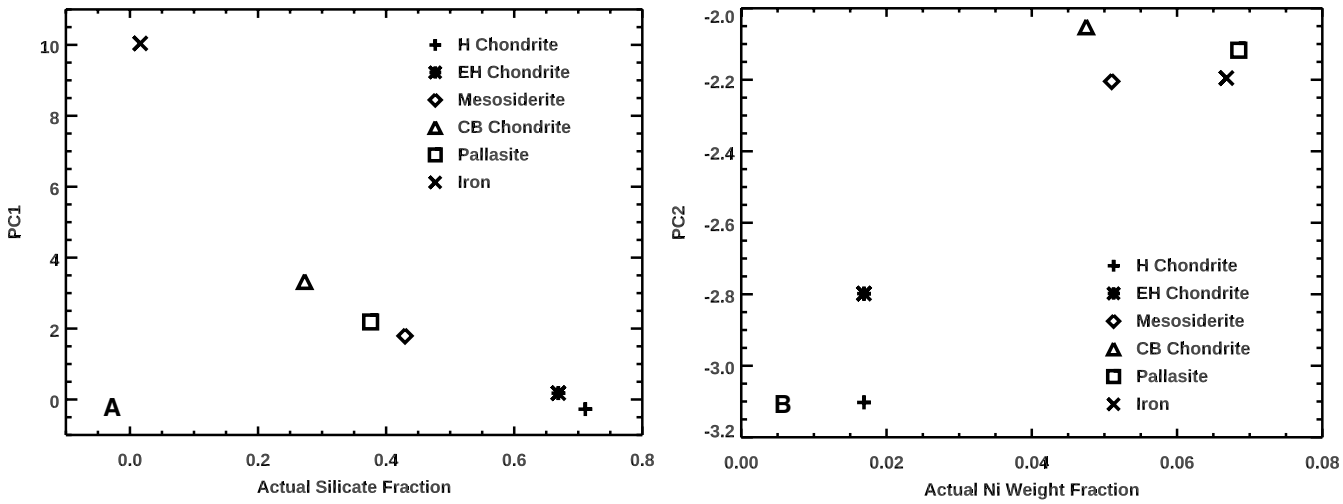

Figure 6. PC1 versus actual silicate values (A), and PC2 versus actual Ni concentrations for the six meteorite compositions given in Table 2.

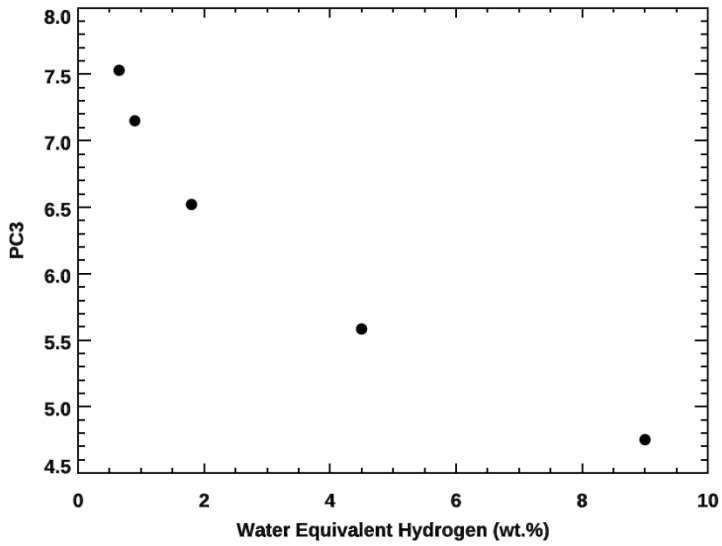

Figure 7. PC3 versus actual water equivalent hydrogen abundances for the five different Mars compositions shown in Figure 5D.

586

587 **References:**

588 Agee, C. B., et al. (2013), Unique Meteorite from Early Amazonian Mars: Water-Rich Basaltic
589 Breccia Northwest Africa 7034, *Science*, *339*(6121), 780-785, doi:10.1126/science.1228858.

590 Beck, A. W., D. J. Lawrence, P. N. Peplowski, T. H. Prettyman, T. J. McCoy, H. Y. McSween,
591 M. J. Toplis, and N. Yamashita (2015), Using HED meteorites to interpret neutron and gamma-
592 ray data from asteroid 4 Vesta, *Meteoritics & Planetary Science*, *50*(8), 1311-1337,
593 doi:10.1111/maps.12467.

594 Berlin, J., R. H. Jones, A. J. Brearley, and M. N. Spilde (2008), Determining Bulk Chemical
595 Compositions of Chondrules by Electron Microprobe: Modal Recombination versus Defocused
596 Beam Analyses, *Microscopy and Microanalysis*, *14*, 110 - 111, doi:10.1017/S1431927608084845.

597 Chevrel, S., P. Pinet, Y. Daydou, S. Maurice, D. Lawrence, W. Feldman, and P. Lucey (2002),
598 Integration of the Clementine UV-VIS spectral reflectance data and the Lunar Prospector gamma-
599 ray spectrometer data: A global-scale multielement analysis of the lunar surface using iron,
600 titanium, and thorium abundances, *Journal of Geophysical Research-Planets*, *107*(E12),
601 doi:10.1029/2000JE001419.

602 Elkins-Tanton, L. T., et al. (2020), Observations, Meteorites, and Models: A Preflight Assessment
603 of the Composition and Formation of (16) Psyche, *Journal of Geophysical Research-Planets*,
604 *125*(3), doi:10.1029/2019je006296.

605 Elphic, R. C., D. J. Lawrence, W. C. Feldman, B. L. Barraclough, S. Maurice, A. B. Binder, and
606 P. G. Lucey (2000), Lunar rare earth element distribution and ramifications for FeO and TiO 2 :
607 Lunar Prospector neutron spectrometer observations, *Journal of Geophysical Research*, *105*(E8),
608 20333-20333, doi:10.1029/1999JE001176.

609 Feldman, W., et al. (2004), Gamma-Ray, Neutron, and Alpha-Particle Spectrometers for the Lunar
610 Prospector mission, *Journal of Geophysical Research: Planets*, *109*(E7),
611 doi:10.1029/2003JE002207.

612 Feldman, W. C., B. L. Barraclough, S. Maurice, R. C. Elphic, D. J. Lawrence, D. R. Thomsen, and
613 A. B. Binder (1998a), Major compositional units of the moon: Lunar prospector thermal and fast
614 neutrons, *Science*, *281*(5382), 1489-1493, doi:10.1126/science.281.5382.1489.

615 Feldman, W. C., S. Maurice, A. B. Binder, B. L. Barraclough, R. C. Elphic, and D. J. Lawrence
616 (1998b), Fluxes of fast and epithermal neutrons from Lunar Prospector: Evidence for water ice at
617 the lunar poles, *Science*, *281*(5382), 1496-1500, doi:10.1126/science.281.5382.1496.

618 Feldman, W. C., M. T. Mellon, O. Gasnault, B. Diez, R. C. Elphic, J. J. Hagerty, D. J. Lawrence,
619 S. Maurice, and T. H. Prettyman (2007), Vertical distribution of hydrogen at high northern
620 latitudes on Mars: The Mars Odyssey Neutron Spectrometer, *Geophysical Research Letters*, *34*(5),
621 doi:10.1029/2006gl028936.

622 Feldman, W. C., A. Pathare, S. Maurice, T. H. Prettyman, D. J. Lawrence, R. E. Milliken, and B.
623 J. Travis (2011), Mars Odyssey neutron data: 2. Search for buried excess water ice deposits at
624 nonpolar latitudes on Mars, *Journal of Geophysical Research-Planets*, *116*,
625 doi:10.1029/2011JE003806.

626 Gasnault, O., W. C. Feldman, S. Maurice, I. Genetay, C. d'Uston, T. H. Prettyman, and K. R.
627 Moore (2001), Composition from fast neutrons: Application to the Moon, *Geophysical Research*
628 *Letters*, *28*(19), 3797-3800, doi:10.1029/2001GL013072.

629 Hardersen, P. S., M. J. Gaffey, and P. A. Abell (2005), Near-IR spectral evidence for the presence
630 of iron-poor orthopyroxenes on the surfaces of six M-type asteroids, *Icarus*, *175*(1), 141-158,
631 doi:10.1016/j.icarus.2004.10.017.

632 Lawrence, D. J., W. C. Feldman, R. C. Elphic, J. J. Hagerty, S. Maurice, G. W. McKinney, and T.
633 H. Prettyman (2006), Improved modeling of Lunar Prospector neutron spectrometer data:
634 Implications for hydrogen deposits at the lunar poles, *Journal of Geophysical Research*, *111*(E8),
635 E08001, doi:10.1029/2005JE002637.

636 Lawrence, D. J., V. R. Eke, R. C. Elphic, W. C. Feldman, H. O. Funsten, T. H. Prettyman, and L.
637 F. A. Teodoro (2011), Technical comment on "Hydrogen mapping of the lunar South Pole using

638 the LRO neutron detector experiment LEND", *Science*, *334*(6059), 1058,
639 doi:10.1126/science.1203341.

640 Lawrence, D. J., et al. (2013a), Evidence for water ice near Mercury's north pole from
641 MESSENGER Neutron Spectrometer measurements, *Science*, *339*(6117), 292-296,
642 doi:10.1126/science.1229953.

643 Lawrence, D. J., P. N. Peplowski, T. H. Prettyman, W. C. Feldman, D. Bazell, D. W. Mittlefehldt,
644 R. C. Reedy, and N. Yamashita (2013b), Constraints on Vesta's elemental composition: Fast
645 neutron measurements by Dawn's gamma ray and neutron detector, *Meteoritics & planetary*
646 *science*, *48*(11), 2271-2288, doi:10.1111/maps.12187.

647 Lawrence, D. J., P. N. Peplowski, A. W. Beck, W. C. Feldman, E. A. Frank, T. J. McCoy, L. R.
648 Nittler, and S. C. Solomon (2017), Compositional terranes on Mercury: Information from fast
649 neutrons, *Icarus*, *281*, 32-45, doi:10.1016/j.icarus.2016.07.018.

650 Lawrence, D. J., et al. (2019), The Psyche Gamma-Ray and Neutron Spectrometer: Update on
651 Instrument Design and Measurement Capabilities, in *50th Lunar and Planetary Science*
652 *Conference*, edited, p. Abstract #1544, Houston, Texas.

653 Lingenfelter, R. E., W. N. Hess, and E. H. Canfield (1961), Lunar Neutron Flux, *Journal of*
654 *Geophysical Research*, *66*(9), 2665-2671, doi:10.1029/JZ066i009p02665.

655 Maurice, S., D. J. Lawrence, W. C. Feldman, R. C. Elphic, and O. Gasnault (2004), Reduction of
656 neutron data from Lunar Prospector, *Journal of Geophysical Research*, *109*(E7), E07S04,
657 doi:10.1029/2003JE002208.

658 Maurice, S., W. Feldman, B. Diez, O. Gasnault, D. J. Lawrence, A. Pathare, and T. Prettyman
659 (2011), Mars Odyssey neutron data: 1. Data processing and models of water-equivalent-hydrogen
660 distribution, *Journal of Geophysical Research*, *116*(E11), E11008-E11008,
661 doi:10.1029/2011JE003810.

662 Peplowski, P. N., D. Bazell, L. G. Evans, J. O. Goldsten, D. J. Lawrence, and L. R. Nittler (2015a),
663 Hydrogen and major element concentrations on 433 Eros: Evidence for an L- or LL-chondrite-like
664 surface composition, *Meteorit. Planet. Sci.*, *50*(3), 353-367, doi:10.1111/maps.12434.

Peplowski, P. N., D. J. Lawrence, W. C. Feldman, J. O. Goldsten, D. Bazell, L. G. Evans, J. W. Head, L. R. Nittler, S. C. Solomon, and S. Z. Weider (2015b), Geochemical terranes of Mercury's northern hemisphere as revealed by MESSENGER neutron measurements, *Icarus*, *253*, 346-363, doi:10.1016/j.icarus.2015.02.002.

Peplowski, P. N., D. J. Lawrence, A. W. Beck, M. Burks, N. L. Chabot, J. O. Goldsten, J. Wilson, and Z. Yokley (2018), Nuclear Spectroscopy of Asteroid 16 Psyche, in *49th Lunar and Planetary Science Conference*, edited, p. Abstract #2114, Houston, TX.

Peplowski, P. N., T. J. McCoy, M. Liebel, A. W. Beck, M. T. Burks, L. T. Elkins-Tanton, D. J. Lawrence, and T. H. Prettyman (2019), Gamma-Ray Spectroscopy of Metal-Rich Meteorites: Preparations for The Psyche Gamma-Ray Spectroscopy Investigation, in *50th Lunar and Planetary Science Conference*, edited, p. Abstract #1731, Houston, Texas.

Peplowski, P. N., and K. Stockstill-Cahill (2019), Analytical Identification and Characterization of the Major Geochemical Terranes of Mercury's Northern Hemisphere, *Journal of Geophysical Research-Planets*, *124*(9), 2414-2429, doi:10.1029/2019JE005997.

Peplowski, P. N., Z. W. Yokley, M. Liebel, S. Cheng, R. C. Elphic, S. F. Hoogerheide, D. J. Lawrence, and J. S. Nico (2020), Position-dependent neutron detection efficiency loss in He-3 gas proportional counters, *Nuclear Instruments & Methods in Physics Research Section a-Accelerators Spectrometers Detectors and Associated Equipment*, *982*, doi:10.1016/j.nima.2020.164574.

Prettyman, T. H., J. J. Hagerty, R. C. Elphic, W. C. Feldman, D. J. Lawrence, G. W. McKinney, and D. T. Vaniman (2006), Elemental composition of the lunar surface: Analysis of gamma ray spectroscopy data from Lunar Prospector, *Journal of Geophysical Research*, *111*(E12), E12007-E12007, doi:10.1029/2005JE002656.

Prettyman, T. H., et al. (2012), Elemental Mapping by Dawn Reveals Exogenic H in Vesta's Regolith, *Science*, *338*(6104), 242-246, doi:10.1126/science.1225354.

Prettyman, T. H., et al. (2013), Neutron absorption constraints on the composition of 4 Vesta, *Meteorit. Planet. Sci.*, *48*(11), 2211-2236, doi:10.1111/maps.12244.

692 Prettyman, T. H., et al. (2017), Extensive water ice within Ceres' aqueously altered regolith:
693 Evidence from nuclear spectroscopy, *Science*, *355*(6320), 55-58, doi:10.1126/science.aah6765.

694 Reddy, V., D. J. Lawrence, L. T. Elkins-Tanton, and D. Takir (2018), Constraining Hydrogen
695 Abundance on Asteroid (16) Psyche, in *49th Lunar and Planetary Science Conference*, edited, p.
696 Abstract #1344, Houston, Texas.

697 Sanchez, J. A., V. Reddy, M. K. Shepard, C. Thomas, E. A. Cloutis, D. Takir, A. Conrad, C.
698 Kiddell, and D. Applin (2017), Detection Of Rotational Spectral Variation On The M-Type
699 Asteroid (16) Psyche, *Astron. J.*, *153*(1), doi:10.3847/1538-3881/153/1/29.

700 Takir, D., V. Reddy, J. A. Sanchez, M. K. Shepard, and J. P. Emery (2017), Detection Of Water
701 And/Or Hydroxyl On Asteroid (16) Psyche, *Astron. J.*, *153*(1), doi:10.3847/1538-3881/153/1/31.

702 Wilks, D. S. (2011), *Statistical Methods in the Atmospheric Sciences, Third Edition*, 676 pp.,
703 Academic Press, Amsterdam, The Netherlands.

704 Wilson, J. T., D. J. Lawrence, P. N. Peplowski, and W. C. Feldman (2019), MESSENGER Gamma
705 Ray Spectrometer and Epithermal Neutron Hydrogen Data Reveal Compositional Differences
706 Between Mercury's Hot and Cold Poles, *Journal of Geophysical Research-Planets*, *124*(3), 721-
707 733, doi:10.1029/2018je005871.

708 Yamashita, N., et al. (2013), Distribution of iron on Vesta, *Meteoritics & Planetary Science*,
709 *48*(11), 2237-2251, doi:10.1111/maps.12139.
710